The Star Formation History of the Blue Compact Dwarf Galaxy UGCA 290¹

Mary M. Crone

Skidmore College, Saratoga Springs, NY 12866, USA

mcrone@skidmore.edu

Regina E. Schulte-Ladbeck

University of Pittsburgh, Pittsburgh, PA 15260, USA

rsl@phyast.pitt.edu

Laura Greggio

Osservatorio Astronomico di Bologna, Bologna, Italy, and Universitätssternwarte München, München, FRG

greggio@usm.uni-muenchen.de

Ulrich Hopp

Universitätssternwarte München, München, FRG

hopp@usm.uni-muenchen.de

ABSTRACT

We present the star formation history of UGCA 290, a galaxy with properties intermediate between Blue Compact Dwarfs and Dwarf Irregulars. This galaxy is particularly interesting because its young stellar population is extremely similar to that of the well-studied type iE Blue Compact Dwarf VII Zw 403, despite its different spatial morphology and old stellar content. Our Hubble Space Telescope/Wide Field Planetary Camera 2 single-star photometry for UGCA 290 extends over nine magnitudes in I, and allows a detailed study of its star formation history. Using synthetic color-magnitude diagrams, we show that the recent "burst" which gives this galaxy its BCD status is a moderate enhancement in star formation which lasted for approximately 20 Myr, at a rate about ten times above its previous rate. The star formation history for most of the previous billion years is consistent with a constant rate, although enhancements as large as

the current one are possible at times ealier than 400 Myr ago. We estimate that the total mass converted into stars in UGCA 290 more than one billion years ago is about three times the astrated mass since that time. The initial mass function is consistent with a Salpeter slope, and the stellar metallicity is bracketed by $Z_{\odot}/50$ and $Z_{\odot}/5$, with evidence for metallicity evolution. Similar results for the star formation history over the past 600 Myr apply to VII Zw 403. Our main result is that despite the traditional picture of BCDs, the current bursts in these two galaxies are neither remarkably intense nor short-lived, and that most of their star formation occured more than a billion years ago.

Subject headings: Galaxies: compact — galaxies: dwarf — galaxies: evolution — galaxies: individual (UGCA 290 = Arp 211, UGC 6456 = VII Zw 403) — galaxies: stellar content

1. INTRODUCTION

The discovery of two extremely low-metallicity blue dwarf galaxies by Searle & Sargent (1972) launched efforts to determine whether such galaxies are young "in the sense that most of their star formation has occurred in recent times" or alternatively, whether "star formation in them occurs in intense bursts which are spearated by long quiescent periods." Their primary argument was that the current level of star formation would quickly overproduce heavy elements, at least according to a Salpeter initial mass function. The category of Blue Compact Dwarf (BCD) has since grown to encompass galaxies with a wide range of morphologies, including galaxies identified through spectral lines, as well as color and compactness (Thuan & Martin 1981). The categories of HII galaxies and amorphous galaxies, while reflecting different selection criteria, apparently have very similar intrinsic properties to BCDs (Marlowe, Meurer, & Heckman 1999).

Much of the interest in BCDs springs from the first possibility: that BCDs are young. As such, their existence would support the delayed formation of dwarfs scenario, in which ionization of the intergalactic medium inhibits star formation in systems with shallow gravitational wells (e.g. Babul & Rees 1992). They would also provide nearby, observationally convenient examples of "primordial" galaxy formation. However, deep CCD imaging in the

¹Based on observations made with the NASA/ESA Hubble Space Telescope, obtained at the Space Telescope Science Institute, which is operated by the Association of Universities for Research in Astronomy, Inc., under NASA contract NAS 5-26555.

1980s ruled out the possibility that the majority of BCDs began forming stars within the last billion years, revealing red elliptical background sheets of presumably older stars (e.g. Loose & Thuan 1986; Kunth, Maurogordato, & Vigroux 1988). Indeed, several of these sheets have now been resolved into red giant stars, implying star formation at least 1-2 Gyr ago (e.g. Schulte-Ladbeck, Crone, & Hopp 1998; Lynds et al. 1998; Schulte-Ladbeck et al. 2000; Drozdovsky et al. 2001). Some authors still claim that the most extreme BCDs — those with especially low metallicities — formed very recently, even as recently as 100 Myr ago (Izotov & Thuan 1999, Izotov et al. 2000). But this possibility is dwindling as well; red background sheets continue to be discovered (e.g. Pox 186; Doublier et al. 2000), and single-star photometry of the most low-metallicity BCD on record suggests stars at least as old as 500 Myr (I Zw 18; Aloisi, Tosi & Greggio 1999; Östlin 2000).

The alternative possibility of intense repeated bursts is problematic also. This scenario requires the existence of a large population of quiescent counterparts to BCDs, but no such population has been clearly identified despite considerable effort (Kunth & Östlin 2000). In fact, several additional lines of evidence point to the possibility that most BCDs are not really bursting in the traditional sense of very short flashes separated by very long quiescent states. Those with resolved stars do not show evidence of long gaps in their recent star formation history (although a short gap is possible in I Zw 18; Aloisi et al. 1999), nor do they exhibit very large star formation rates, only in the range 10^{-3} to 10^{-2} M_{\odot}yr⁻¹ (Schulte-Ladbeck et al. 2001). Large-scale surveys support the conclusion that star formation rates for BCDs are typically less than $0.3 \, \mathrm{M}_{\odot} \mathrm{yr}^{-1}$ (Popescu, Hopp, & Rosa 1999). Thus, the nature of the BCD designation, including the details of the current burst and the relationship to other gas-rich dwarfs with less intense levels of star formation, is still a puzzle.

To address these questions, we obtained Wide Field Planetary Camera images of UGCA 290, the most nearby BCD without a large red background sheet. Up to this point, all BCDs resolved as deeply as the red giant branch were of the common subtype iE, in which the star forming region is embedded in a large elliptical background of older, red stars. Ground-based images of UGCA 290, on the other hand, show that its star formation extends over a large fraction of the visible galaxy, in the form of two large lobes. Single-star photometry of a BCD with this different kind of morphology provided us the opportunity to gain insight into the general nature of the BCD designation.

In a recent Letter, we presented our V,I color-magnitude diagram from these data (Crone et al. 2000). We found a red giant branch, corresponding to a spatially compact population of stars older than 1-2 billion years, within which the current star formation is embedded. From the magnitude of the tip of the red giant branch we found a distance of 6.7 Mpc, and distance-dependent parameters $M_B = -13.4$ and $L\alpha = 1.2 \times 10^{39}$ erg s⁻¹.

Overall, we found that the properties of UGCA 290 are intermediate between those of BCDs and Dwarf Irregulars. We also noted that its bright stellar content is extremely similar to that of the well-studied iE BCD VII Zw 403, despite its different spatial morphology and old stellar content.

Here we present our full HST photometry of UGCA 290 in the filters F336W, F555W, F814W, and F656N. We then investigate its nature using synthetic color-magnitude diagrams, addressing the meaning of the BCD designation through the details of the current burst and its earlier star formation history. Our main conclusion is that neither of the two scenarios proposed by Searle & Sargent fits the nearby BCDs UGCA 290 and VII Zw 403.

2. OBSERVATIONS AND REDUCTION

We observed UGCA 290 in August of 1999 as part of GO program 8122. We obtained data in four filters: F814W, F555W, F336W, and F656N. For F814W and F555W, which approximate I and V, we took six 1300 s exposures, at three dither positions, for a total of 7800 s in each filter. For F336W and F656N we obtained two 1300 s exposures at one position, for a total of 2600 s in each filter.

We combined exposures at the same pointings using CRREJ and then combined the dithered images using DRIZZLE onto a 1600 × 1600 pixel grid. The drizzling procedure allowed us to recognize and remove cosmic rays left by CRREJ (which have a characteristic basketweave shape in the drizzled image because they do not appear in all three dither positions) and hot pixels missed by WARMPIX (which appear as three diagonally spaced hotspots.) Figure 1 shows the color image of the PC, along with a ground-based image we obtained at the Calar-Alto 1.23 m telescope. We captured most of the galaxy within the WFPC2 field, but missed part of the lower surface brightness region to the northeast. Note that the galaxy is quite transparent — see the two red background galaxies — and free of bright HII regions. The two lobes of star formation which give the galaxy a bimodel appearance are the large regions in the upper left and lower right.

After masking out a few obvious background galaxies, we conducted single-star photometry with DAOPHOT. We took the zero points from the May 1997 SYNPHOT tables and determined our point spread function (PSF) from relatively isolated stars in our images. With no drizzling, the full width at half maximum of the PSF is 0.07 arcseconds for the PC chip and 0.13 arseconds for the WF chips, in each filter. The drizzling procedure for the F555W and F814W filters produces better defined but marginally larger PSFs, with a full width at half maximum of 0.08 arcseconds for the PC chip and 0.15 arcseconds for the WF

chips. Figure 2 shows the DAOPHOT errors from the PSF fitting procedure. Note that we do not see as deeply in the F336W filter, partly because of our shorter exposure time and lack of dithering in this filter.

We estimated the completeness of our photometry by adding artificial stars to our images using ADDSTAR, and checking to see what percentages of them we could recover. In order to maintain the same level of crowding as in the original, we created simulated images by adding 5% of the observed number of resolved stars, consistent with their observed luminosity function. We created 200 such images for each filter in two different regions: in the PC chip, to model the more crowded inner part of the galaxy; and in the quarter of the WF2 chip closest to UGGA 290, to model the background sheet. We considered a star to be recovered if the difference between its input magnitude and recovered magnitude was less than 0.7 mag. Figure 2 includes the results of these tests. In most cases, the completeness for the more sparsely populated WF2 chip is better than for the PC chip, despite its inferior resolution; only for bright stars in the F336W filter is this trend significantly reversed. Completeness tests also provide an estimate of error: the difference between the added magnitudes and recovered magnitudes of the false stars (Figure 2, bottom row). Note the systematic brightening at faint magnitudes, presumably because of blending with nearby stars. This effect cannot be modeled using simply the DAOPHOT errors, which provide an rms value only. DAOPHOT errors are also less likely to take into account correctly stars which overlap concentrically. For these reasons, we use the false star errors rather than the DAOPHOT errors in the analysis which follows.

We corrected for the small foreground extinction in this direction according to Schlegel et al. (1999), assuming an $R_{\rm V}=3.1$ extinction curve: $A_{\rm U}=0.076,\ A_{\rm V}=0.046,\ A_{\rm R}=0.037,\ {\rm and}\ A_{\rm I}=0.027.$ We have not attempted to correct for extinction within UGCA 290, but its transparency outside major regions of star formation suggests that it is low, at least for stars in the background sheet. Finally, we transformed our F555W and F814W magnitudes into ground-based V and I following Holtzman et al. (1995). We chose not to transform the F336W band into U, because of the larger uncertainties in this transformation (Holtzman et al. 1995). Finally, we cross-identified stars among different filters requiring spatial coincidence within the full width at half maximum of the PSF.

3. STELLAR CONTENT

Our deepest images come from the long, dithered exposures in V and I. Figure 3 shows our V, I color-magnitude diagram (CMD), along with that of the well-studied iE BCD VII Zw 403. (Our reduction of the VII Zw 403 data is described in Schulte-Ladbeck et al.

1998). The CMD for each galaxy includes the entire region of active star formation and most of the red background sheet, and therefore approximately reflects the star formation history of the entire galaxy. To help interpret the nature of the hottest stars in the diagram, whose V-I colors are less sensitive to temperature, we incorporate information from the F336W filter as well. Stars with F336W-F555W color less than -1.0 are colored blue, those between -1.0 and 0.0 green, those between 0.0 and 1.0 yellow, and those greater than 1.0 red. Stars in black were not detected in F336W. The absolute luminosity scale is set by the magnitude of the tip of the red giant branch (TRGB), as described in Crone et al. 2000.

Several features are clear in both CMDs. The abundance of very blue stars (V-I<0)suggests a strong main sequence up to $M_I = -6$, while the slight redward turn of the blue plume at very bright magnitudes suggests post-main sequence stars older than a few Myr. Unfortunately, there is no clear separation in the lower blue plume between main sequence stars and blue He-burning stars. There is a mix of F336W-F555W colors within the blue plume. For example, among the very brightest stars in UGCA 290 are ones color-coded both yellow and blue. This effect is not simply due to photometric errors, which are less than 0.2 mag in F336W-F555W for these stars; it probably reflects the presence of stars in different evolutionary phases coexisting on the V, I CMD. It is also possible that some stars with anomalous colors are actually binary systems of bright, differently colored stars. The blue plume population for VII Zw 403 contains a slightly larger population of very hot stars (color-coded blue) than that for UGCA 290. A well-defined red plume at 1.0 < V - I < 2.0peaks at about the same magnitude as the blue plume, and is smoothly populated down to the tip of the asymptotic giant branch at $M_I \sim -5$. The red giant branch occupies the region redward of $V-I\sim 0.5$ and faintward of $M_I\sim -4$. In the case of VII Zw 403, the red giant branch is very heavily populated, and there are many asymptotic giant branch (AGB) stars between $M_I = -4$ and -5, magnitudes expected for ages between about 600 Myr and 1200 Myr. This large older population occupies an elliptical sheet several kpc across, surrounding the compact (< 1 kpc) star forming region (Schulte-Ladbeck et al. 1999). This is typical of the type iE BCD morphology. In contrast, a relatively small number of these older stars appear in UGCA 290, and their spatial distribution is much smaller relative to the star forming region (Crone et al. 2000). Despite these differences in older populations, however, the younger populations are clearly similar.

To quantify this similarity, we performed a two-dimensional Kolmogorov-Smirnov (K-S) test using the subroutines in Press et al. (1992), with significance levels determined using a bootstrap normalization for our particular data (see, for example, the procedure in Fasano & Franceschini 1987). A fair comparison of the two CMDs using this test requires that errors and completeness issues do not affect the two distributions differently; we limited the data to the region $M_I < -4$, $M_V < -3.7$, for which completeness is better than 95%

and photometric errors are smaller than 0.09 in each filter. This region includes 424 stars for UGCA 290 and 408 stars for VII Zw 403. (Note that the K-S test is designed to find differences in distribution rather than total number of points.) We find that the stars in this region, which stretch over nearly five magnitudes, are not distinguishable using the K-S test. If we extend the comparison region of the CMD to include even a small bit of the older stars in the red giant branch or asymptotic giant branch, the K-S test easily distinguishes the distributions. For example, shifting the cutoff down to $M_{\rm I} < -4$, $M_{\rm V} < -3.0$ results in distributions that are different at the 99.9% level.

Another simple quantitative measure of the two stellar populations is their luminosity function. Figure 3 includes the completeness-corrected I-band luminosity functions of the blue and red plumes, split in color at V-I=0.7. We fit each histogram to the function $\log N = \log N_{\rm o} + \alpha M_{\rm I}$, again limiting ourselves to magnitudes where the photometry is better than 95% complete ($M_{\rm I} < -4$ for the blue plume and $M_{\rm I} < -5.5$ for the red plume). In all cases, this function provides a good fit, with a reduced chi-squared of less than 1.5. As expected from the K-S test results, the slopes for the two galaxies are consistent with each other. For the blue plume, the slopes α are 0.44 ± 0.03 for UGCA 290 and 0.49 ± 0.03 for VII Zw 403. For the red plume, they are 0.22 ± 0.05 and 0.26 ± 0.06 , respectively. The histograms also highlight the slightly greater population of bright stars in UGCA 290 brighter than $M_{\rm I} = -6$, and the significantly greater populations of red giants and asymptotic giant branch stars in VII Zw 403. The total number of stars in the faintest magnitude bins are extremely sensitive to completeness estimates and are therefore difficult to compare.

Figure 4 presents our full results for F336W, potentially valuable not only for interpreting the hottest stars but also for estimating extinction. Before discussing this figure, we caution that for several reasons the F336W data are more difficult to interpret than the data in F555W and F814W. As noted above, the transformation between F336W and U is rather uncertain, depending on stellar surface gravity and, for redder stars, the red leak in the F336W filter. Combined with our shorter exposure time and lack of dithering, these limitations prompt us to focus our quantitative study on V and I, and view the F336W information as supplemental.

Still, the F336W filter can provide some useful information. In Figure 4, color-coding indicates M_I magnitude, and is helpful for identifying stars with their position on the V-I color-magnitude diagram. Stars with $M_I < -8$ are represented in blue, $-8 < M_I < -6$ in green, $-6 < M_I < -4$ in yellow, and $M_I > -4$ in red. The bright end of the blue plume in F336W, F555W is better defined for VII Zw 403; note how the bright (e.g. green-colored) stars are more concentrated at blue F336W-F555W color. This corresponds to the higher proportion of very hot, bright stars in VII ZW 403 visible in Figure 3. The K-S test applied

to the region above the dashed line in Figure 4 distinguishes the bright populations to better than 99% certainty.

In the color-color diagrams, the main features are the cluster of mostly fainter (redcolored) stars at F336W-F555W ~ -1.5 , $V - I \sim -0.2$ and the tail of mostly brighter stars extending downward. Note that the cluster of faint stars extends to redder F336W-F555W colors in the case of VII Zw 403; this is because the F336W data are deeper for VII Zw 403, allowing us to see the fainter, redder stars at $M_V \sim -3.5$, F336W-F555W ~ -1.3 . The arrows show a reddening vector for E(B-V)=0.5, according to the extinction curve of Cardelli, Clayton, & Mathis (1989). Lynds et al. (1998), compare their color-color diagram of VII Zw 403 (based on these same data) with a theoretical isochrone for metallicity Z=0.008 and age 4 Myr, transformed into the F336W, F555W system according to Holtzman et al. (1995). They conclude that there is very little internal reddening in this galaxy. (Note that we do find a stream of about a dozen stars coming from the main cluster of VII Zw 403 in the direction of the reddening vector, which probably does indicate substantial reddening for these few stars.) Given the similarities of these two color-color diagrams, the same result would hold for UGCA 290. In some cases it is useful to determine the differential reddening of each star and then correct the CMDs for this effect. We prefer not to do this. For one thing, these stars are in different, unknown evolutionary phases. For example, the colors of the three stars at $(V-I)_o \sim 1.5$ could be either negligibly reddened red plume stars or heavily reddened main sequence stars. And again, the transformation to the F336W filter is rather uncertain. In any case, there is very little evidence for reddening. Along the downward tail, for example, there is only about 0.3 mag of scatter. Photometric errors alone reach about 0.1 in the F336W filter for these stars, and as high as 0.5 mag for the fainter stars in the main cluster.

For the purposes of our theoretical modelling, we will focus on our superior images in V and I, with the following input from the F336W filter: little evidence of systematic reddening, a scatter indicating differential reddening of less than $E(B-V) \sim 0.3$, with a few outliers; and a mix of stars with different temperatures along the blue plume.

4. COMPARISON TO SYNTHETIC COLOR-MAGNITUDE DIAGRAMS

4.1. Procedure

To interpret the star formation history in more detail, we employ synthetic colormagnitude diagrams which include theoretical stellar evolutionary tracks and atmospheres, convolved with errors and completeness fractions to mimic our data. Specifically, we use the Bologna code (Greggio et al. 1998) with the Padova tracks (Fagotto et al. 1994) and the atmospheres of Bessell, Castelli, & Pletz (1998).

Estimates of errors and completeness are provided by false star tests, as described in Section 2. There are some sources of error, however, that are not included in these tests. One is differential reddening, which is likely to cause some scatter in the CMD towards redder colors and fainter magnitudes. We do not expect this to be a large effect for this particular galaxy, because of its high galactic latitude, its intrinsic transparency (Figure 1), and because there is little evidence for it in our color-color diagrams (Figure 4). Another is the clustering properties of the stars, including the importance of compact young clusters and binaries. Although we perform completeness tests for both a more crowded "star formation" region and a less crowded "background sheet" region, we do not lay down stars precisely according to their actual clustering properties. In fact, no matter how careful the analysis, one cannot perfectly determine the clustering properties of the stars directly from the image.

Recently some authors have presented methods to automate the process of finding the best-fit synthetic CMDs (e.g. Harris & Zaritsky 2001.) These methods are suited to situations where theoretical predictions and observational errors are very well quantified, such as high-resolution images of nearby galaxies, and well-understood features on the CMD. Because our best data are for very young and metal-poor stars with relatively poorly constrained positions on the CMD and uncertainties which are difficult to quantify, we prefer to use a more "hands-on" approach. Our basic procedure is to consider a series of boxes in color and magnitude which include stars of progressively older ages, as described in detail below. We used the same kind of procedure in Schulte-Ladbeck et al. (2001). Similarly, we do not expect to find very a precise solution for initial mass function (IMF) and metallicity, but instead expect to find a fairly wide range of these parameters consistent with the data.

In order to examine the likely range of metallicities for this galaxy, we consider a low value of Z=0.004 ($Z_{\odot}/50$, the lowest measured HII region abundance), and a higher value of Z=0.004 ($Z_{\odot}/5$). There are no published nebular metallicities for this galaxy, so this choice of upper limit is guided by the appearance of the CMD. As illustrated in Figure 5a, the stellar populations are likely to be bracketed by these two values, with the bright young stars closer to Z=0.004 and the older red giant branch stars closer to Z=0.0004. Indeed, in Crone et al. (2000) we estimated from the red giant branch a low stellar metallicity $[Fe/H] = -2.0 \pm 0.1$, which in turn suggests a low nebular metallicity $12 + \log(O/H) \sim 7.6$, or Z=0.001. We can also use the fact that the young stars have very similar colors to those in VII Zw 403, which has a measured nebular metallicity (O/H) between $Z_{\odot}/20$ and $Z_{\odot}/10$ (Martin 1997; Izotov, Thuan, & Lipovetsky 1997; Izotov & Thuan 1999). Finally, the simple fact that UGCA 290 is as faint as $M_B = -13.4$ also suggests $12 + \log(O/H) \sim 7.6$ (Skillman,

Kennicutt, & Hodge 1989). For each metallicity we consider a power law IMF, $\xi \propto M^{-\alpha}$ with the slope α in the range 1.35 to 3.35, the standard Salpeter IMF (Salpeter 1955) being 2.35. The star formation rates we quote in this section assume a constant slope from 0.1 M_{\odot} to 100 M_{\odot} .

We model the star formation history using boxes such as those illustrated in Figure The basic idea is to consider a series of regions on the CMD which include stars of progressively older ages. The choice of box location and size is guided by identifying regions which have both well-determined ages and large enough populations to provide a precise estimate of the SFR. To identify such regions, we performed a series of simulations showing the appearance of an aging coeval burst. We found, for example, that for the Z=0.004 model the stars in Box B are between about 10 and 15 Myr old, so that the total number of these stars can be used to determine the star formation rate over this time period. The stars produced along with those in Box B must then be taken into account when considering the next box. We used the boxes in Figure 5b to determine the star formation rates for the Z=0.004 models in the periods 0-10 Myr ago (Box A), 10-15 Myr ago (Box B), 15-20Myr ago (Box C), 20 - 50 Myr ago (Box D), 50 - 1000 Myr ago (Box E), and more than 1 Gyr ago (Box F). Note that although we use Box A, which includes the tip of the main sequence, to constrain the youngest population, this box may also contain stars as old as 100 Myr; therefore, during the modeling procedure we use it after Box E. Note also that the time resolution goes down dramatically for Boxes E and F, because populations with a wide range of ages (and which are not well-constrained elsewhere on the CMD) cohabit these regions of the CMD. Finally, random fluctuations produce a wide range of star formation rates for boxes with few stars. Not all of these rates are consistent with other parts of the CMD — for example, some random realizations based on Box B overproduced the lower part of the main sequence at $M_I \sim -4$. Only those rates which produced acceptable results overall contributed to our determination of the star formation rates and the uncertainties in these rates. We do not use the very faintest magnitudes, those with completeness estimates of less than 50%, to constrain the models.

4.2. The Star Formation History: Basic Features

Before discussing the star formation history in detail, we describe some overall features of our results. The model which best matches our data has a Salpeter IMF and a metallicity which evolves from the lower value $Z_{\odot}/50$ for the RGB stars to the higher value $Z_{\odot}/5$ for the youngest stars. Figure 6 illustrates the SFH over the past Gyr for this model. The burst peaks 10 - 15 Myr ago at 0.042 ± 0.010 M_{\odot}yr⁻¹, and then decreases to about one fourth

of this rate. Before the burst, the rate is about one tenth of this. Each bin in Figure 10 represents the average SFR determined using one of the boxes in Figure 5. The bins for relatively recent times represent boxes with good time resolution but fewer stars, resulting in narrower bins with larger errors bars. The bins for later times represent boxes with many stars of a wide range of ages, cohabiting the same part of the CMD. Each bin represents a kind of average for the SFR within the time period under consideration; there can be unresolved fluctuations in the SFR within these periods. We do not include results for times earlier than 1 Gyr, because we lose nearly all time resolution at this point. Section 4.5 below describes the constraints we can put on the SFR prior to this time.

The differences between our best model and the data are not surprising given the known uncertainties. Figure 7 shows one of the random realizations of our best model. This figure excludes stars with V-I < 2.0 in an attempt to exclude thermally-pulsing AGB stars from our analysis; the simulator does not place these stars on the CMD because the colors and lifetimes in this phase are not theoretically well-determined. The data scatter to redder colors than the theoretical model, an effect expected from differential reddening. This trend is especially obvious for the very brightest supergiants, whose theoretical colors are also affected by uncertainties in the theoretical temperatures for massive post-main sequence stars (Renzini et al. 1992). Second, there are slightly more very faint stars in the data. These low luminosity bins are very sensitive to incompleteness and could well represent an inadequacy in our completeness estimate. Alternatively, it could reflect a slightly steeper luminosity function, or an enhancement in star formation several 100 Myr ago, possibilities which we discuss below. Third, there is a discontinuity in color in the blue plume at $M_I \sim -6$. There are two effects which likely come into play to "smooth out" this feature. Differential reddening (and any additional blending we have missed) would tend to smooth out such sharp features. Indeed, both synthetic plumes are sharper than the data. Also, the relative time spent in the blue and red parts of the blue loops is quite model-dependent (see Renzini et al. 1992). Figure 8 illustrates the dependence on metallicity by showing a model using low-Z tracks only. In contrast to the high-Z model, this one overproduces blue-loop stars in the blue plume around $M_I \sim -6$. A metallicity slightly lower than Z=0.004 might therefore explain the lack of stars here in our best model. There are clearly other difficulties with the low-Z model. Most strikingly, it cannot reproduce the brightest stars because of their very short lifetimes; even with an IMF as top-heavy as 1.35 we were still unable to reproduce the very bright stars without vastly overproducing the fainter stars.

Our best model has a Salpeter IMF. A slope as steep as 3.00 clearly overproduces faint, blue main sequence stars relative to the brightest supergiants (Figure 9). Similarly, a slope as flat as 1.35 clearly fails to produce enough main sequence stars relative to the brightest supergiants (Figure 10).

To summarize, the basic features of the CMD support our guess that the metallicity is bracketed by Z=0.004 and Z=0.0004, with the young stars closer to Z=0.004. The IMF slope is close to Salpeter, and is certainly bracketed by 1.35 and 3.00. In the detailed description of the SFH which follows, we will describe the robustness of our results with the respect to this range of parameters.

4.3. The Recent Starburst

The recent burst peaked 10-15 Myr ago at $0.042 \pm .010$ M_{\odot}yr⁻¹, and then decreased to about one fourth of this rate. Before the burst, the rate was about one tenth of this. Each of these features in the SFH can be understood in terms of general features in the CMD. The very recent level must produce a main sequence as bright as $M_{\rm I} \sim -6$ while not overproducing very bright, blue supergiants relative to red supergiants. The intensity and duration of the enhancement, as well as those of the pre-burst phase, must produce a smoothly populated red plume brightward of $M_{\rm I} \sim -6$. If the burst had started earlier, for example, the red plume below $M_{\rm I} \sim -8$ would be overpopulated (Figure 11). If, on the other hand, the SFR had been constant at the rate 50 Myr ago, with no burst at all, there would not be nearly enough main sequence stars or bright supergiants (Figure 12).

Models with different IMFs result in slightly different burst parameters. A steeper IMF, which has a relatively greater number of low mass stars, is skewed toward relatively higher rates for recent times, because these rates are constrained by more massive stars on the CMD. For $\alpha = 3.00$, the burst rises from $0.3 \pm 0.1~{\rm M}_{\odot}{\rm yr}^{-1}$ in the interval $15-20~{\rm Myr}$ ago, peaks at $0.6 \pm 0.2~{\rm M}_{\odot}{\rm yr}^{-1}$ from $10-15~{\rm Myr}$ ago, then decreases to one third of the peak value; before the burst, the rate is only about 1/20 the burst rate. Therefore, the burst is effectively shorter and more intense. This should be taken as an extreme limit to the burst intensity. For the flatter slope $\alpha = 1.35$, the effect is the opposite. The burst remains constant over the $10-20~{\rm Myr}$ period at $0.01~{\rm M}_{\odot}{\rm yr}^{-1}$, then decreases to a current rate of one eighth this value; before the burst the rate is just five times lower than the burst rate. This should be seen as a lower limit to the burst intensity. In both cases, extending the burst as far back as 50 Myr results in an unacceptable buildup of stars in the red plume.

The low-Z model does such a poor job producing the very brightest stars that it does not provide much meaningful input on burst parameters. It does provide one very general result, however: as with the other models, if the burst continues as long as 50 Myr, there is an unacceptable buildup of stars in the red plume.

4.4. The Intermediate Star Formation History

Over the long period from 1 Gyr ago all the way up to 50 Myr ago, the data are consistent with a constant star formation rate, at a rate about one half that of the pre-burst phase (one third for the steep IMF and the same rate for the flat IMF). However, moderate fluctuations can easily "hide" in the data. We performed simulations in which we added a burst similar to the recent one at various times in the past, to see if we could detect them. Specifically, we added a 20 Myr burst at $0.04~\rm M_\odot~\rm yr^{-1}$ which begin at 100 Myr, 200 Myr, 300 Myr, 400 Myr, 500 Myr, and 1 Gyr. While the two most recent times clearly conflict with the data, a burst as recent as 300 Myr ago effects primarily the lowest magnitude bins, and at 400 Myr ago, the differences could be interepreted as inadequate completeness estimates (Figure 13). A burst at 500 Myr adds only 100 stars to the synthetic CMD, and one at 1 Gyr adds only 30. Remember that even our "best model" slightly overproduces faint stars, an effect which we attributed to incompleteness in our discussion above. If, instead, we trust our completeness estimate totally, this difference could mean a reduced SFR somewhere in the period 200-500 Myr ago. We could, for example, decrease the SFR by a factor of one half for the period 450-500 Myr ago.

Likewise, we cannot rule out periods of total quiescense. Although significant gaps in star formation are ruled out for more recent times — we find that gaps as large as 10 Myr within the past 50 Myr clearly disagree with the data — large gaps may have occurred at earlier times. Figure 14 illustrates an extreme example. In this model there is no star formation in the period 500-1000 Myr ago, and yet the model CMD matches the data nearly as well as our best model. There is only a slight overproduction of faint blue Helium-burning stars, because we raised the star formation rate slightly in the period 50-500 Myr ago to compensate for the loss of red plume stars otherwise produced 500-1000 Myr ago. A similar type of compensation allows a 100-Myr gap as recently as the period 100-200 Myr ago. These uncertainties highlight the difficulty in determining a precise SFH for intermediate times without an unambiguously identified blue He-burning branch.

4.5. Early Star Formation History

A small part of the UGCA 290 red background sheet extends into the WF2 chip, and a slightly larger part of the background sheet is missed by the WFPC2 entirely (see Figure 1, and Karachentsev & Makarov 1998). Therefore, the results for this phase of the SFH require modeling of data in both the PC and WF chips. We illustrate our modeling of this older population using the WF data, because these are less contaminated by young stars. Figure 15a shows the CMD for the quarter of the WF2 chip nearest the galaxy center, inluding 300

stars. There is no indication that the galaxy extends into other parts of the WFPC2 field of view. Far from the main body of the galaxy there are only a few stars, in a random spatial distribution and with intermediate V-I colors atypical for the rest of the galaxy. We use the farthest quarter of the WF3 chip to provide an estimate of the contamination in the WF2 (Figure 15b).

We model the WF2 data using the errors and completeness estimates specific to this chip. The main feature is the RGB, but there are a few other stars, beyond those expected from contamination, which suggest a low level of more recent star formation. We do not see deeply enough down the RGB to distinguish details of the SFH earlier than 1 Gyr ago. Instead we consider four different models with constant star formation at a rate fixed to produce the right number of stars at the TRGB (specifically, within Box F of Figure 5). We model two different starting times: an "old" model, starting 10 Gyr ago, and a "young" model, starting only 2 Gyr ago. We use both the "high" metallicity Z=0.004 model and the "low" metallicity Z=0.0004 model. Figure 16 shows an example for each set of parameters. In addition to the stars older than 1 Gyr, we include in each diagram the "contamination" stars from Figure 15b and the results of a simulation with constant star formation at 0.0001 M_{\odot} for the past 1 Gyr.

To aid in comparing the models, we also plot in Figure 16 the distribution in color at the TRGB, within the region $0.8 < (V - I)_o < 2.3$, $-4 < M_I < -3$. The low-Z models successfully match the blue edge of the TRGB, but do not extend to red enough colors. The high-Z models, on the other hand, match the red edge of the TRGB but do not extend to blue enough colors. Thus, the width of the TRGB is larger than one would expect simply from our photometric errors. The most likely explanation is metallicity evolution. It is also possible that differential reddening contributes to this effect. The models clearly rule out the possibility that the bulk of the stars are both old and have the higher metallicity, although we cannot rule out old low-Z stars or young high-Z stars. Unfortunately, we cannot determine from these data when UGCA 290 first began to form stars.

Regardless of the time when star formation first began, we can address the question of whether the galaxy is "young" in the sense that it formed *most* of its stars recently — for example, within the past 1 Gyr. To do this we compare the total astrated mass before and after 1 Gyr ago, for the entire galaxy. This is a fairly straightforward application of our CMD models. Using the SFRs cited above, the total astrated mass within the last 1 Gyr comes to $2.8 \times 10^6 \,\mathrm{M}_{\odot}$ for the PC with a negligibly small contribution from the outer parts of the galaxy. The total astrated mass earlier than 1 Gyr ago is in the range $4-10 \times 10^6 \,\mathrm{M}_{\odot}$ in the PC and $1-2 \times 10^6 \,\mathrm{M}_{\odot}$ in the WF2. The higher masses correspond to higher metallicity and higher age. As already noted, our HST observations miss the northeast edge of the

red background sheet, a region about half the area of the PC chip. If we assume that the population on this edge of the background sheet is the same as that on the southern edge in the WF2, we can scale our results using the flux in our R-band ground based image. Using the region on the ground based image farthest from the galaxy to estimate a background correction, we find that the flux of the part missed by the WFPC2 is 1.6 to 2.0 times the flux in the region we see in the WF2. Therefore, to get the total star formation rate of the galaxy, we add the value for the PC chip to 2.6 - 3.0 times the value for the WF2 chip. The total astrated mass more than a billion years ago is thus $7-16\times10^6~{\rm M}_{\odot}$, which is two to six times that since. For the $\alpha = 3.00$ models, where rates are skewed higher for recent times relative to the Salpeter IMF models, the astrated mass before a billion years ago is still two to three times higher than that since. For $\alpha = 1.35$, where rates are skewed lower for recent times, the astrated mass before a billion years ago is five to twenty times higher than that since. If star formation began earlier than 10 Gyr ago, the astrated mass is higher than otherwise. For example, For $\alpha = 2.35$ and star formation beginning 15 Gyr ago, the astrated mass before a billion years ago is six to nine times higher than that since. Therefore, UGCA 290 formed most of its stars more than a billion years ago. In this sense, it is not "young."

Another way to compare quantitatively the early SFH with the more recent SFH is through the birthrate parameter SFR/ < SFR $>_{past}$, where the numerator represents the average SFR over a recent time period — for example, the past billion years — and the denomenator represents the average SFR earlier than this (see Schulte-Ladbeck et al. 2001). In these terms, the birthrate parameter for UGCA 290 ranges from about 0.4 to about 4.0 depending on age, metallicity and IMF. For a Salpeter IMF and the low metallicity Z=0.0004, it is 0.5 for a 2-Gyr old galaxy and 2.5 for a 10-Gyr old galaxy. If we extend the SFH back to 15 Gyr ago, the birthrate parameters are about the same as for the 10-Gyr case; although the primary effect of lengthening the period of star formation is to reduce the average rate, there is also the competing effect that the total astrated mass is higher in models where star formation begins earlier. For comparison, our modeling of HST/Near Infrared Camera photometry for the BCD galaxies Mrk 178 (Schulte-Ladbeck et al. 2000) and I Zw 36 (Schulte-Ladbeck et al. 2001) both produced slightly larger birthrate parameters on the order of ten.

4.6. Summary of Synthetic Modeling

We consider the following our robust results: The recent "burst" which granted UGCA 290 its BCD status is an enhancement of about ten times the previous star formation rate during

the past 1 Gyr, peaking at a rate of $0.04 \pm 0.01 \,\mathrm{M_{\odot}yr^{-1}}$. It has lasted for about 20 Myr, and not longer than 50 Myr. The current star formation rate is likely to be a few times lower than the peak of the burst. Over the long period from 1 Gyr up to 50 Myr ago, the SFR is consistent with a constant rate, but modulations as large as the recent burst can hide for times earlier than 400 Myr ago, as can quiescent periods hundreds of millions of years long. The blue side of the tip of the red giant branch agrees with a low metallicity Z=0.0004, while its red extension suggests metallicity evolution. The number of stars at the TRGB, scaled to the entire galaxy using the R-band image, indicates that the total mass astrated before 1 Gyr ago is several times the total astrated mass since then.

5. SPATIAL DISTRIBUTION OF THE RECENT ENHANCEMENT

There are several questions about the history of UGCA 290 which can be addressed by the spatial distribution of resolved stars, including whether there is any evidence of propagating star formation, and whether the galaxy represents an interacting pair or recent merger. Figure 17 illustrates the spatial distribution of stars of progressively older ages. From left to right, the stars were selected to have formed during the burst (the past 20 Myr), the preburst phase (20 to 50 Myr ago), the intermediate period (50 Myr to 1 Gyr ago), and the early period (more than 1 Gyr ago). We have attempted to select as many stars as possible without contamination by stars of different ages. Based on our best model, this means $M_{\rm I} < -7.5$ (very bright supergiants) or $M_{\rm I} < -4, V - I < -0.2$ (main sequence stars); $-7.5 < M_{\rm I}$ and $M_{\rm I} < -6.0$, V - I > 0.2; $-6.0 < M_{\rm I} < -4.5$ and V - I > 0.2; and $M_{\rm I} > -4.0$ and V - I > 1.0. The last category may include AGB stars as young as 500 Myr along with the older stars. The most obvious trend, not suprisingly, is that the older stars are more dispersed. The structure of the burst is clearer in Figure 18, where we zoom in on the star forming region. The two large lobes are obvious (the northern lobe looks like a double cluster), but there are also more widely distributed stars, which are between the two main lobes, forming two bubble-like shapes. On the right panel of Figure 18 we overlay the burst stars with the diffuse H_{α} distribution from our F656N images. To produce contours of the diffuse gas, we subtracted point sources from the continuum-subtracted image and smoothed to a scale of 30 pc. The large-scale H α morphology of UGCA 290 is clearly different from that in more typical BCDs such as VII Zw 403, which show bright knots surrounding young stars (e.g. Crone et al. 2001). Instead, the burst stars appear on the edges of two large regions with diffuse emission. There are no bright stars visible within the most intense knots of $H\alpha$ emission, despite their relatively low surface brightness. It is tempting to guess that the young stars have blown away the gas out of which they formed.

To address the relationship of the two large lobes of star formation, we examine their individual CMDs (Figure 19). The stellar content in these two regions is similar, the most obvious differences being the red AGB stars in the South lobe and the small space in the blue plume at I=23 in the North lobe. The K-S test, applied to the entire CMD (including 862 stars in the south lobe and 842 stars in the north lobe), shows a 10% probability that they are drawn from the same distribution. Thus, there is no compelling evidence that star formation is propagating from one region to the other, or that they represent different objects which are merging or interacting. On the contrary, the burst seems to be a large-scale phenomemon over the entire central region of the galaxy.

6. DISCUSSION AND CONCLUSIONS

Our main result is that the recent "bursts" in both UGCA 290 and VII Zw 403 are not especially extreme, and that we see no evidence for long gaps in star formation in their recent history. These results are similar to those for other nearby BCDs resolved with HST. The star formation rates we determine from these galaxies are on the order of $10^{-3}-10^{-2}~M_{\odot}~{\rm yr}^{-1}$ (see the review in Schulte-Ladbeck 2001). Indeed, the only late-type dwarf whose resolved stellar population indicates a major burst is NGC 1569 (Greggio et al. 1998). As reviewed by Tosi (2001), this galaxy has a SFR per unit area of $\sim 4~M_{\odot}~{\rm yr}^{-1}{\rm kpc}^{-2}$, which is $\gtrsim 40$ times the rate in other nearby late-type dwarfs. In these units, UGCA 290 (with a star forming region about 1 kpc across), has 0.01 $M_{\odot}~{\rm yr^{-1}kpc^{-2}}$ and VII Zw 403 (with a star forming region about 0.5 kpc across; Crone et al. 2000) has 0.02 M_{\odot} yr⁻¹kpc⁻². Likewise, we do not see evidence for major gaps in star formation in nearby BCDs. For example, we find that for a sample of four BCDs observed with HST/NICMOS, very long gaps in star formation (> 1 Gyr) could not have occurred just prior to the current burst (Schulte-Ladbeck et al. 2001). Therefore, the traditional picture of intense bursts and long gaps does not seem to apply to nearby BCDs. This is not entirely surprising. The distances to most BCDs are not precisely known, making it difficult to obtain accurate estimates of their star formation rates. Moreover, the statistics obtained for relatively distant BCDs are subject to a Malmquist bias, producing a higher average SFR than would a volume-limited sample. Finally, it now appears likely that the metallicity in BCDs is significantly affected by preferential loss of enriched gas and infall of low-metallicity gas (see Kunth & Östlin 2000 for a review).

The star formation history from our CMD modeling is quantitatively consistent with the few other observations available for UGCA 290. From our continuum-subtracted F565N image, its H α flux is $2.0 \pm 0.3 \times 10^{-13}$ erg s⁻¹ cm⁻², which for an extinction of 0.1 mag

corresponds to a luminosity of 1.21×10^{39} erg s⁻¹. Using the conversion in Hunter & Gallagher (1986) for a Salpeter IMF from $0.1 \rm M_{\odot}$ to $100 \rm M_{\odot}$, the star formation rate is then $0.0085 \pm$ $0.002~{\rm M_{\odot}yr^{-1}}$. This is consistent with the rate $0.011\pm0.008~{\rm M_{\odot}yr^{-1}}$ we derive here from the resolved stars. We can also check for consistency between our astrated mass and the dynamical mass of UGCA 290 from H α and HI spectroscopy. For a Salpeter IMF, we derive an astrated mass of $9.6-18.4\times10^6~{\rm M}_{\odot}$. Considering IMF slopes in the range 1.35 to 3.00 broadens this range to $9.6-63.5\times10^6~{\rm M}_{\odot}$. If 30% of the mass is recycling to the interstellar medium through stellar winds and supernova, the current stellar mass comes to about $7-13\times10^6$ M_{\odot}, and possibly as high as 40×10^6 M_{\odot}. These estimates are based on a single-slope IMF down to a mass of $0.1 M_{\odot}$. For an IMF which flattens for low masses, as observed in the galactic disk, the total astrated mass decreases. For example, if the slope between $0.1-0.6~\mathrm{M}_{\odot}$ is -0.564 (Gould, Bahcall, & Flynn 1997), the astrated mass decreases by factors of 0.9, 0.6, and 0.5 for slopes of 3.00, 2.35, and 1.35, respectively. The total mass of course includes loose gas as well. We can estimate the neutral gas using the integrated HI flux of UGCA 290 S=2.18 Jy km/s (Karachentsev, private communication). Using the standard formula $M_H = 2.36 \times 10^5 d^2S$, where S is the flux in Jy km/s, d is the distance in Mpc, and the mass is in solar masses, we obtain $2.3 \times 10^7 \rm{M}_{\odot}$. This is several times higher than the stellar mass for a Salpeter slope. We can also make a very rough estimate of the ionized gas mass from the H α flux. Following Clayton (1987), and assuming a gas volume of 1 kpc³ and a filling factor of 0.1, the mass in ionized hydrogen is about $3 \times 10^4 M_{\odot}$, which is negligible compared to the other sources of mass. A lower limit to the total dynamical mass can be derived from the rotation curve. Using the $H\alpha$ line (Karachentsev & Makarov 1998), which shows a rotation velocity of about 12 km/s at a radius of 20 arcseconds (650 pc, at our distance), the formula $M_{\rm T} = V^2(R)RG^{-1}$ yields a lower limit of $3.4 \times 10^7 {\rm M}_{\odot}$ approximately the sum of the stellar and gas masses. More precise mass estimates, and in particlar a solid estimate of the dark matter content, await new observations.

Combining these estimates of the star formation history and total gas content of UGCA 290, we can also address its gas consumption timescale. A very short gas consumption timescale implies that the current level of star formation cannot be maintained for a long period, and is one of the traditional arguments for the unusual nature of BCDs. For UGCA 290, the maximum burst level of $\sim 0.04~M_{\odot}~\rm yr^{-1}$ would take 600 million years to use up its HI gas mass, even at 100% efficiency. In fact, this "burst" level was maintained for only $\sim 15~\rm Myr$. The average star formation rate of UGCA 290 over the past billion years, $\sim 0.003~M_{\odot}~\rm yr^{-1}$, could be maintained for over seven billion years. Therefore, UGCA 290 may well continue forming stars in a similar manner for a long time.

Thanks to the similarity between the bright stellar contents in UGCA 290 and VII Zw 403, we can compare our results for the recent burst to observations of the latter galaxy as well.

Recall that the bright stars in the V, I CMDs of these two galaxies (including Boxes A through D, and the main sequence down to $M_{\rm I}=-4$), have essentially the same distribution. The total number of stars in this region is nearly the same also, VII Zw 403 having 96% the number of stars in UGCA 290. Because the models were constrained using regions which are not significantly different in the two galaxies, the results for UGCA 290 are consistent with the VII Zw 403 data as well. (Compare the histograms in Figure 3 with those in Figure 7). There are two pieces of information which are not included in these statistical comparisons, which suggest that the current rate is slightly higher in VII Zw 403: the higher proportion of very hot stars revealed in F336W, and the higher numbers of main sequence stars in the very lowest magnitude bins (which are, however, very sensitive to an accurate determination of completeness). The current SFR for VII Zw 403 may therefore be on the high side, but should still be within the uncertainties we determined from our models. From the continuum-subtracted F656N images of VII Zw 403 (part of the same observations described in Schulte-Ladbeck et al. 1999), we find a flux of $7.6 \times 10^{-13} \text{ erg s}^{-1} \text{ cm}^{-2}$. For a distance of 4.4 Mpc and 0.1 mag extinction, this corresponds to a luminosity 1.9×10^{39} erg s⁻¹, or a star formation rate of $0.014~{\rm M_{\odot}yr^{-1}}$. This rate does agree with our value of $0.011\pm0.008~{\rm M_{\odot}yr^{-1}}$ from the resolved stars. Lynds et al. modeled the intermediate and old star formation history of VII Zw 403 and concluded that the heavy AGB above the TRGB corresponds to a major episode of star formation which lasted for 200 – 600 Myr and ended about 600 Myr ago. In the case of a 200 Myr burst, the burst level would be about 30 times the level after the burst. We emphasize that this burst does not have to be even this intense if it is longer. We also emphasize that the current burst — the burst which gives VII Zw 403 its BCD appearance — is a much shorter and more recent phenomenon.

The similarity of the recent bursts in UGCA 290 and VII Zw 403 poses the question of whether they have the same physical cause. Indeed, the causes of BCD bursts in general are not clear. Pustilnik et al. (2001) conclude that most BCDs are triggered by tidal interactions or mergers, although VII Zw 403 is one of the exceptions in their sample. Unfortunately, it is often difficult to judge whether a galaxy might be interacting because of poor distance determinations, difficulty in observing faint companions, and ambiguous merger morphologies. Even in the case of UGCA 290, where we can study the spatial distribution of burst stars in detail, it is not clear what caused the burst. One might interpret its fairly moderate nature as support for the idea that we are simply catching it in a relatively active phases of an internal stochastic process, but this is not necessarily so.

The behavior of these two galaxies fits neither of the scenarios outlined in Searle and Sargent; the recent bursts are not especially intense or brief, and most of their star formation occurred more than a billion years ago. In addition, the IMF slope appears to be close to Salpeter, at least for the massive stars. Our growing knowledge of BCDs suggests that we

should switch to a picture of moderate enhancements instead of major bursts — a picture that would solve the problem of the missing "quiescent" counterparts, which need not be so very different from BCDs themselves. Our results highlight, rather than solve, another part of the BCD puzzle: the cause of the recent enhancements in star formation. Are they triggered externally, or simply part of an internal stochastic process? What intrinsic properties are required of a gas-rich dwarf for it to take part is such events?

We thank I. Karachentsev for providing us with HI data for UGCA 290. Work on this project was supported through HST grants to RSL and MMC (project 8122), and by the Charles Lubin Chair at Skidmore College. We used NASA/IPAC Extragalactic Database, operated by the Jet Propulsion Laboratory, California Institute of Technology, under contract with NASA.

REFERENCES

- Aloisi, A., Tosi, M, & Greggio, L. 1999, AJ, 118, 302
- Bessell, M.S., Castelli, F., & Plez, B. 1998, A&A, 337, 321
- Babul, A., & Rees, M.J. 1992, MNRAS, 255, 346
- Crone, M.M., Schulte-Ladbeck, R.E., Hopp, U., & Greggio, L. 2000, ApJ, 545, L31
- Crone, M.M., Schulte-Ladbeck, R.E., Hopp, U., & Greggio, L. 2001, in "Dwarf Galaxies and Their Evinronment", eds K.S. de Boer, R.J. Dettmar, U. Klein, Shaker Verlag; in press
- Cardelli, J.A., Clayton, G.C., & Mathis, J.S. 1989, ApJ, 345, 243
- Clayton, C.A. 1987, MNRAS, 266, 493
- Doublier, V., Kunth, D., Courbin, F., & Magain, P. 2000, A&A, 353, 887
- Drozdovsky, I.O., Schulte-Ladbeck, R.E., Hopp, U., Crone, M.M., & Greggio, L. 2001, ApJ, 551, L135
- Fagotto, R., Bressan, A., Bertelli, G., & Chiosi, C. 1994, A&AS, 105, 29
- Fasano, G., & Franceschini, A., 1987, MNRAS, 225, 155
- Gould, A., Bahcall, J.N., & Flynn, C. 1997, ApJ, 482, 913
- Greggio, L, Tosi, M., Clampin, M., De Marchi, G., Leitherer, C., Nota, A., Sirianni, M. 1998, ApJ, 504, 725.
- Harris, J. & Zaritsky, D. 2001, ApJS, 136, 25
- Holtzman, J.A., Burrows, C.J., Casertano, S., Hester, J.J., Trauger, J.T., Watson, A.M. & Worthey, G. 1995, PASP, 107, 1065
- Hunter, D.A. & Gallagher, J.S. 1986, PASP, 98, 5
- Izotov, Y.I., Thuan, T.X. 1999, ApJ, 511, 639
- Izotov, Y.I., Thuan, T.X., & Lipovetsky, V.A. 1997, ApJS, 108, 1
- Izotov, Y.I., Papderos, P., Thuan, R.X., Fricke, K., Foltz, C., & Guseva, N. 2000, in "The First Stars," ESO Astrophysics Symposia, eds. A. Weiss, T. Abel, & V. Hill (Springer), 303

Karachentsev, I.D. & Makarov, D.I. 1998, A&A, 331, 891

Kunth, D., Maurogordato, S., & Vigroux, L. 1988, A&A, 204, 10

Kunth, D. & Östlin, G. 2000, A&A Rev., 10, 1

Loose & Thuan, T.X. 1986, in Star-Forming Dwarf Galaxies and Related Objects, Ed. D. Kunth, T.X. Thuan, & J.T.T. Van (Gif-Sur-Yvette: Editions Frontieres), 73

Lynds, R., Tolstoy, E., O'Neil Jr, E.J., Hunter, D.A. 1998, AJ, 116, 146

Marlowe, A.T., Meurer, G.R., Heckman, T.M. 1999, ApJ, 522, 183

Martin, C. 1997, ApJ, 491, 561

Östlin, G. 2000, ApJ, 535, L99

Popescu, C.C., Hopp, U., Rosa, M.R. 1999, A&A 350, 414

Press, W.H., Teukolsky, S.A., Vetterline, W.T., & Flannery, B.P. 1992, Numerical Recipes, Second Edition (Cambridge University Press)

Pustilnik, S.A., Kniazev, A.Y., Lipovetsky, V.A., & Ugryumov, A.A 2001, A&A, 373, 24

Renzini, A., Greggio, L., Ritossa, C., & Ferrario, L. 1992, ApJ, 400, 280

Salpeter, E.E. 1955, ApJ, 121, 161

Schlegel, D.J., Finkbeiner, D.P., Davis, M. 1998, ApJ, 500, 525

Schulte-Ladbeck, R.E., Hopp, U., Greggio, L., Crone, M.M., Drozdovsky, I.O., & Hopkins, A.M. 2001, in "Dwarf Galaxies and their Environment", eds K.S. de Boer, R.J. Dettmar, U. Klein, Shaker Verlag; in press

Schulte-Ladbeck, R.E., Crone, M.M., & Hopp, U. 1998, ApJ, 493, L23

Schulte-Ladbeck, R.E., Hopp, U., Crone, M.M., Greggio, L. 1999, ApJ, 525, 709

Schulte-Ladbeck, R.E., Hopp, U., Greggio, L., & Crone, M.M. 2000, AJ, 120, 1713

Schulte-Ladbeck, R.E., Hopp, U., Greggio, L., Crone, M.M., & Drozdovsky, I. 2001, AJ, 121, 3007

Searle, L. & Sargent, W.L.W. 1972, ApJ, 173, 25

Silich, S., Tenorio-Tagle, G., Munoz-Tunon, C., & Cairos, L.M. 2001, astro-ph/0104340

Skillman, E.D., Kennicutt, R.C., & Hodge, P.W. 1989, ApJ, 347, 875

Tosi, M. 2001, in "Dwarf Galaxies and Their Environment", eds. K. S. de Boer, R.J. Dettmar, & U. Klein, Shaker Verlag, in press

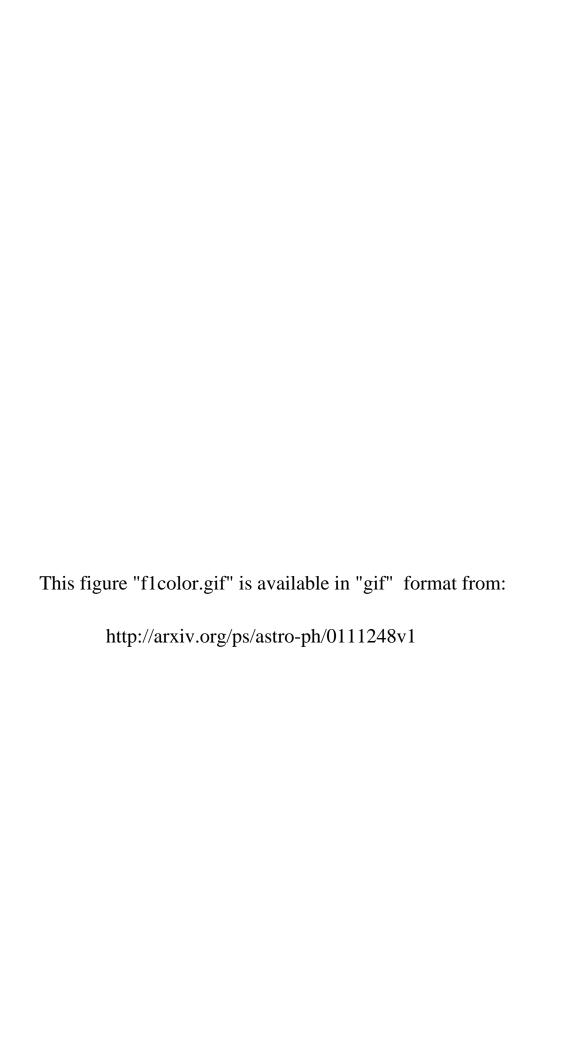
Thuan, T.X., & Martin, G.E. 1981, ApJ, 247, 823

This preprint was prepared with the AAS IATEX macros v5.0.

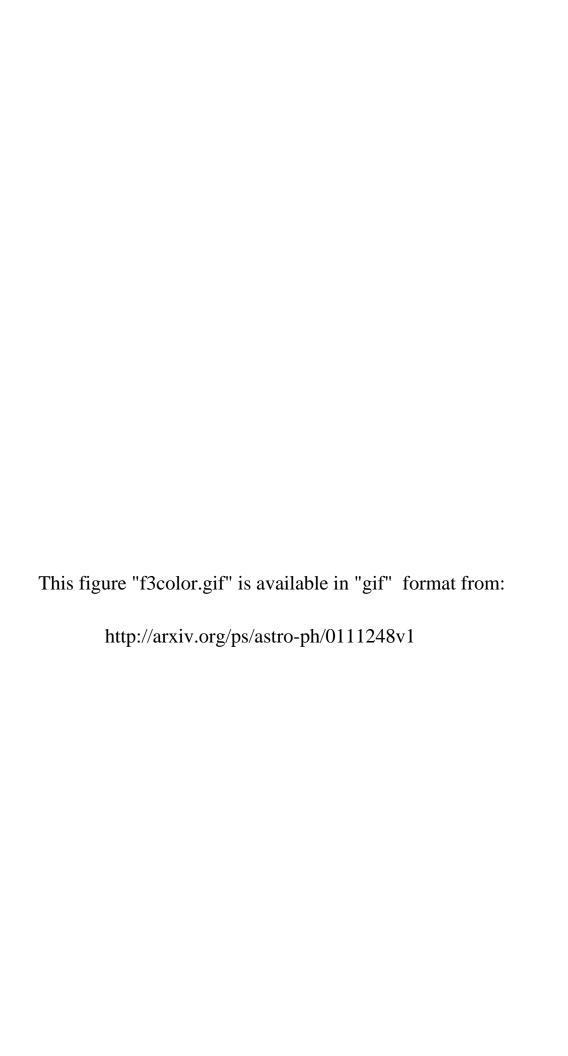
- Fig. 1.— WFPC2 Planetary Camera image, showing the star-forming region of UGCA 290. The inset, our R-band image taken with the Calar-Alto 1.23 m telescope, shows the WFPC2 field of view. For both images, north is to the lower right.
- Fig. 2.— Errors from DAOPHOT (top row), completeness fractions (middle row), and errors from false star tests (bottom row) for our data in the F814W, F555w, and F336W filters. For the completeness fractions, solid lines show results for the PC chip and dashed lines show results for the quarter of the WF2 chip nearest the main body of UGCA 290. For the error plots, the results for both chips are superimposed; the two chips have effectively the same distribution of errors at a given magnitude.
- Fig. 3.— Color-magnitude diagrams in V and I for UGCA 290 and VII Zw 403 (top) and their I-band luminosity functions. Color-coding in the CMDs indicates F336W-F555W color, as explained in the text; stars not detected in F336W are left black. Dashed lines indicate the regions we compare using the K-S test. The diagrams for both galaxies are set to the same absolute magnitude scale. The apparent magnitude scale on the left refers to UGCA 290; the distance modulus for VII Zw 403 is 0.9 mag less. The lower panels show the luminosity functions for both UGCA 290 (bold lines) and VII Zw 403 (fine lines), corrected for incompleteness. On the left are \sqrt{N} error bars for reference.
- Fig. 4.— Color-magnitude diagrams in F336W and F555W (top), and color-color diagrams (bottom). The color-coding indicates I-band magnitude, as explained in the text. All the stars detected in both F336W and F555W were also detected in I. The dotted line in the upper panels show the regions we compare using the K-S test. The arrows in the lower panels are reddening vectors for E(B-V)=0.5 mag.
- Fig. 5.— The PC data superposed with several Padova evolutionary tracks (left) and with boxes used for creating synthetic models (right). The tracks include models with Z=0.004 (red) and Z=0.0004 (blue) for masses 30 M_{\odot} , 12 M_{\odot} , and 1 M_{\odot} .
- Fig. 6.— The recent star formation history of UGCA 290, according to our best model.
- Fig. 7.— The best model, along with the PC data for comparison. Below are the luminosity functions for the data (bold lines) and the model (fine lines). On the left are \sqrt{N} error bars for reference.
- Fig. 8.— The best low-metallicity model, as described in the text. The format is the same as that for Figure 7.

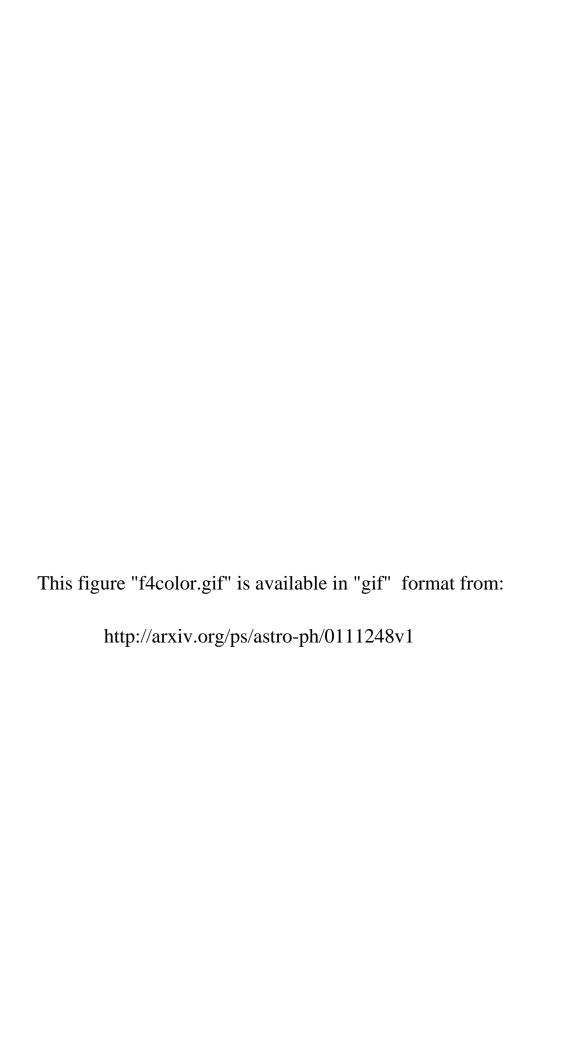
- Fig. 9.— The best model with a steep IMF exponent $\alpha = 3.00$
- Fig. 10.— The best model with a flat IMF exponent $\alpha = 1.35$
- Fig. 11.— Same as the model in Figure 7, except with the recent burst beginning 50 Myr ago instead of 20 Myr ago.
- Fig. 12.— Same as the model in Figure 7, except without a recent burst. Instead, star formation is constant from 50 Myr ago onward.
- Fig. 13.— Same as the model in Figure 7, except with an additional burst at 400 Myr with duration 20 Myr and rate $0.04 \text{ M}_{\odot}\text{yr}^{-1}$. The loss of time resolution this long ago is such that the burst is nearly hidden.
- Fig. 14.— Same as the model in Figure 7, except with a gap in star formation from 500–1000 Myr ago.
- Fig. 15.— Data from the WF chips. The quarter of the WF2 chip closest to the PC (a) includes primarily stars in the red background sheet of UGCA 290 and is considered part of that galaxy. The quarter of the WF3 chip farthest from the PC (b) gives an estimate of contamination by objects not in UGCA 290.
- Fig. 16.— Synthetic models of the WF data. On the left are color-magnitude diagrams. On the right are the distributions in color in the region $0.8 < (V I)_o < 2.3$, $-4 < M_I < -3$ (the tip of the red giant branch.) See text for the model parameters.
- Fig. 17.— Distribution of stars with progressively older ages. From left to right, the age ranges are approximately 0 20 Myr, 20 50 Myr, 50 1000 Myr, and > 1000 Myr. Solid lines indicate the WFPC2 field of view.
- Fig. 18.— Distribution of stars in the recent burst, along with H α contours. The vertical line on the left shows a scale of 1 kpc.

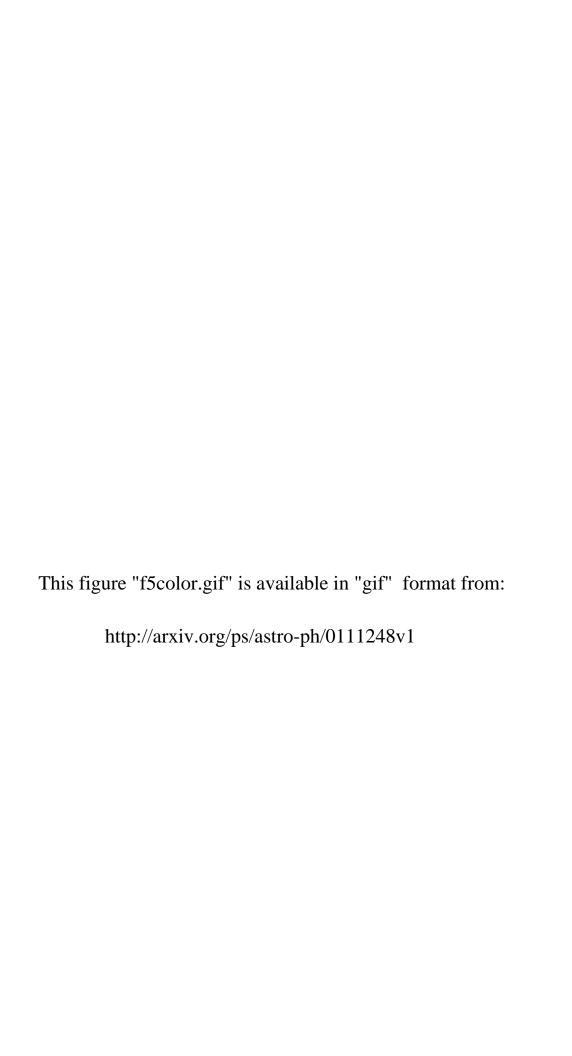
Fig. 19.— The V,I CMD for each of the two major spatial lobes of star formation.

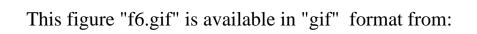


This figure "f2.gif" is available in "gif" format from:





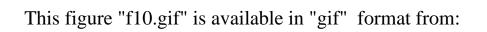




This figure "f7.gif" is available in "gif" format from:

This figure "f8.gif" is available in "gif" format from:

This figure "f9.gif" is available in "gif" format from:



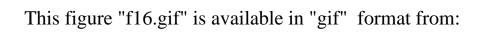
This figure "f11.gif" is available in "gif" format from:

This figure "f12.gif" is available in "gif" format from:

This figure "f13.gif" is available in "gif" format from:

This figure "f14.gif" is available in "gif" format from:

This figure "f15.gif" is available in "gif" format from:



This figure "f17.gif" is available in "gif" format from:

This figure "f18.gif" is available in "gif" format from:

This figure "f19.gif" is available in "gif" format from: